HEALTH AND MEDICINE

Lymph-targeted high-density lipoprotein-mimetic nanovaccine for multi-antigenic personalized cancer immunotherapy

Mingqi Liu†, Yang Feng†, Yougong Lu, Renqi Huang, Ying Zhang, Yanan Zhao, Ran Mo*

Cancer vaccines show huge potential for cancer prevention and treatment. However, their efficacy remains limited due to weak immunogenicity regarding inefficient stimulation of cytotoxic T lymphocyte (CTL) responses. Inspired by the unique characteristic and biological function of high-density lipoprotein (HDL), we here develop an HDL-mimicking nanovaccine with the commendable lymph-targeted capacity to potently elicit antitumor immunity using lipid nanoparticle that is co-loaded with specific cancer cytomembrane harboring a collection of tumor-associated antigens and an immune adjuvant. The nanoparticulate impact is explored on the efficiency of lymphatic targeting and dendritic cell uptake. The optimized nanovaccine promotes the co-delivery of antigens and adjuvants to lymph nodes and maintains antigen presentation of dendritic cells, resulting in long-term immune surveillance as the elevated frequency of CTLs within lymphoid organs and tumor tissue. Immunization of nanovaccine suppresses tumor formation and growth and augments the therapeutic efficacy of checkpoint inhibitors notably on the high-stemness melanoma in the mouse models.

INTRODUCTION

Vaccinations are considered effective preventive interventions against infectious diseases by greatly reducing morbidity and mortality in public health (*1*). Cancer vaccines have been extensively investigated over the past decade, which aim to eliminate cancer cells through tumor antigen–specific cellular immune responses (*2*–*5*). To date, a few prophylactic vaccines have been approved by the U.S. Food and Drug Administration (FDA) and applied for the prevention of malignancies caused by hepatitis B virus and human papillomavirus (*6*). Notably, tumor antigens are endogenously characterized by low immunogenicity and often barely induce effective immune responses (*7*, *8*), which quite differ from traditional vaccines with antigens from foreign pathogens. Moreover, traditional vaccines elicit humoral immunity, whereas cellular immunity mediated by the $CD8^+$ cytotoxic T lymphocytes (CTLs) plays a key role in killing cancer cells for cancer vaccines (*9*, *10*). A variety of strategies have been developed to increase the efficacy of the vaccine by application of the whole-tumor lysate (*11*), coadministration of antigens with adjuvants (*12*, *13*), and formulation in carriers (*14*). Nanocarriers are recognized as promising delivery vehicles for cancer vaccines, which facilitate targeted delivery of antigens to essential immune organs and cell types (*15*–*17*). Secondary lymphoid organs, especially lymph nodes (LNs), are rich in dendritic cells (DCs) and T cells, which are crucial target sites for strong antigen-specific CTL-mediated responses of cancer vaccines. An effective delivery system targeting LNs and DCs is still desired for the development of cancer vaccines (*18*, *19*).

High-density lipoprotein (HDL) is an endogenous nanoparticle for the transportation of lipids, such as cholesterol and triglycerides in the human body, which has varying constituents and characteristics relying upon the maturation phase (*20*). Nascent discoidal HDL is formed by lipidation of apolipoprotein A1 (ApoA1) that is produced in the liver or intestine and absorbs cholesterol ester that is converted from cholesterol by lecithin cholesterol acyltransferase, resulting in the transformation from discoidal to spherical HDL (*21*). A typical mature HDL with a spherical morphology consists of a hydrophobic lipid core and a phospholipid monolayer anchored with ApoA1 (*22*). HDL has been validated to be actively transported into the lymphatic vessels through the scavenger receptor class B type I (SR-BI) expressed on the lymphatic endothelial cells (*23*, *24*). However, the application of endogenous HDL for drug delivery vehicles is limited by the high-cost purification process, the difficulty of large-scale manufacture, and the safety concerns of blood-borne pollution (*25*, *26*). To address this dilemma, HDL-mimicking nanocarriers have been increasingly explored for targeted delivery of therapeutic agents and enhanced efficacy of disease treatment (*27*–*30*). Lipid nanoparticles (LNPs) composed of hydrophobic cores parceled by phospholipids and functionalized with apolipoprotein or apolipoprotein-mimetic peptides attract considerable interest for lymph-targeted drug delivery and cancer vaccination (*31*–*34*). Of note, the efficacy of lymphatic targeting and immune cell uptake of LNPs is highly correlated with their nanoparticle properties (*35*, *36*), such as formulation composition, particle size, and surface charge. However, the relative investigation remains elusive. In addition, cancer stem-like cells (CSCs) that are characterized by self-renewal, high tumorigenicity, and therapeutic resistance are identified as one of the key factors leading to tumor growth and metastasis (*37*, *38*). Cancer vaccine for preventing and treating CSC-derived tumor progression is still lacking.

In this work, we engineered a lymph-targeted HDL-mimicking LNP that is wrapped by a cancer cell membrane carrying the full assay of membrane antigens and loaded with imiquimod (R837), a hydrophobic immune adjuvant (*39*) for a combined prophylactic and therapeutic cancer vaccine. R837, a specific agonist to the Toll-like receptor 7/8 (TLR7/8) (*40*, *41*) is encapsulated in the lipid core

State Key Laboratory of Natural Medicines, Jiangsu Key Laboratory of Drug Discovery for Metabolic Diseases and Jiangsu Key Laboratory of Drug Design and Optimization, Center of Advanced Pharmaceuticals and Biomaterials, School of Life Science and Technology, China Pharmaceutical University, Nanjing 211198, China.
*Corresponding author. Email: rmo@cpu.edu.cn
†These authors contribute equally to this work.

of LNP. The R837-loaded LNP (R837/LNP) is wrapped by the cell membrane with multi-antigens isolated from the cancer cells or the poorly immunogenic CSCs for developing personalized cancer vaccination (R837/LNP-M). An ApoA1-mimetic peptide, named 22A peptide (*29*, *42*), is modified on the surface of R837/LNP-M to acquire the 22A-modified membrane-coated R837-loaded LNP (R837/LNP-M-L) (Fig. 1A). The nanoparticulate properties are modulated by formulation change, such as core composition, particle size, surface charge, and peptide decoration. We explore the nanoparticulate impact on the efficacies of lymphatic targeting and DC uptake in vitro and in vivo (Fig. 1B). The optimized LNP-M-L has a potent capacity for lymphatic targeting and DC uptake. After subcutaneous inoculation, the obtained R837/LNP-M-L markedly promotes the co-delivery of antigens and adjuvant to the LNs and generates effective DC activation and CTL responses (Fig. 1C). Immunization with R837/LNP-M-L delays the tumor formation and growth in the mouse models of melanoma and augments therapeutic efficacy of clinically applied immune checkpoint inhibitors against the stemness-derived immunoresistant melanoma.

RESULTS

Construction of LNP-M-L for lymphatic targeting and DC uptake

LNP was prepared using the nanoprecipitation method. LNP-M was obtained by repeatedly co-extruding LNP and the cell membranes from the mouse melanoma B16F10 adherent cells (ACs). Rational design and formulation optimization are important for LNP-M to be an efficient cancer vaccine. In view of this, we evaluated the impact of nanoparticle properties of LNP-M, including core composition, particle size, surface charge, and peptide modification, on the efficiencies of lymphatic targeting in the mouse models and cellular uptake by the isolated primary DCs. Two fluorescent dyes, lipophilic carbocyanine DiD and coumarin 6 (Cou6), were encapsulated in LNP-M for tracking and determination of in vivo lymphatic targeting and in vitro DC uptake, respectively. The mice were subcutaneously injected with the DiD-labeled LNP-M (DiD/LNP-M) at the tail base. After 24 hours, the mice were euthanized, and the draining LNs were harvested and imaged by In Vivo Imaging System (IVIS). The DCs were isolated from the bone marrow of the mice and incubated with the

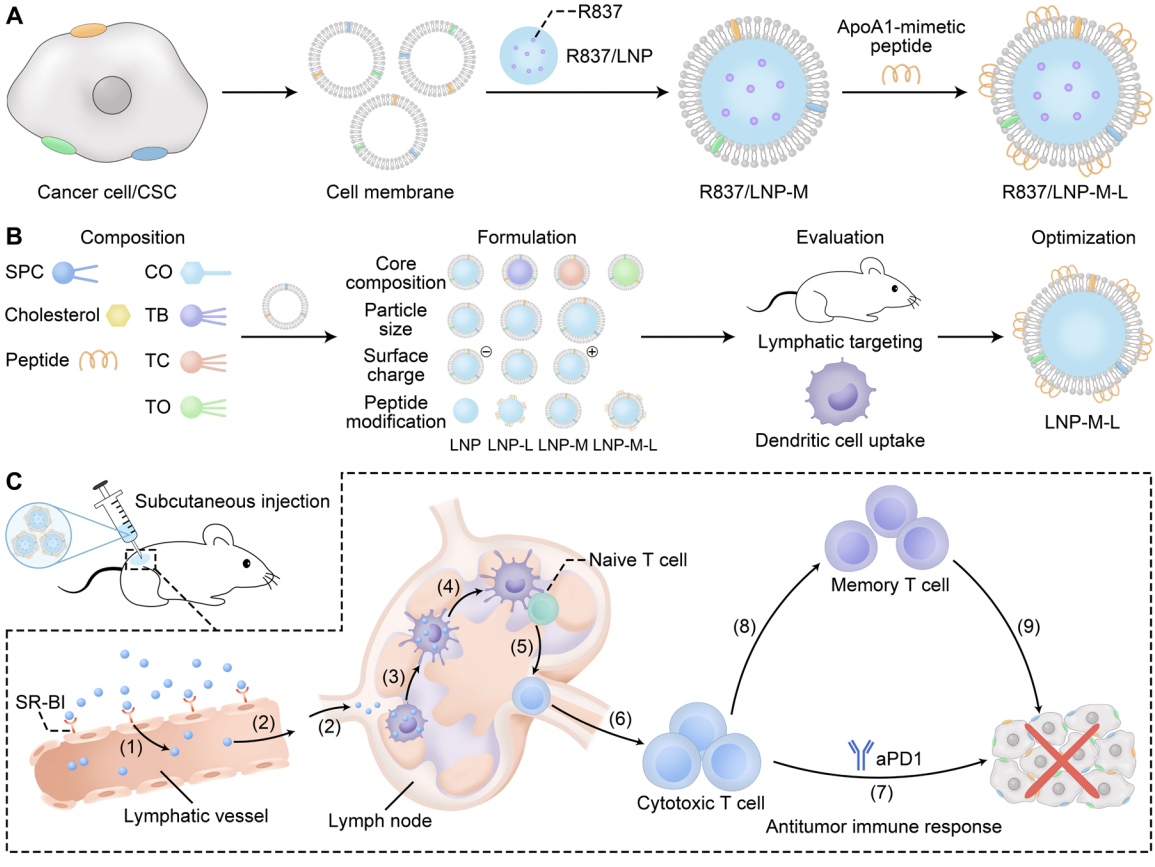

Fig. 1. Schematic of lymph-targeted HDL-mimicking LNP for cancer vaccination and personalized immunotherapy. (**A**) Preparation of R837/LNP-M-L as cancer nanovaccine. R837 is loaded in the lipid core of LNP, which is enveloped by the cytomembrane with tumor-associated antigens isolated from cancer cells or poorly immunogenic CSCs, followed by surface modification with an ApoA1-mimetic 22A peptide. (**B**) Exploration of the nanoparticulate properties of LNP-M including core composition, particle size, surface charge, and peptide modification for in vivo lymphatic targeting and in vitro DC uptake. SPC, soybean phosphatidylcholine; CO, cholesteryl oleate; TB, tributyrin; TC, tricaprin; TO, triolein. (**C**) Antitumor immune responses elicited by vaccination of R837/LNP-M-L. (1) After subcutaneous injection, R837/LNP-M-L permeates the lymphatic vessel via the SR-BI–mediated manner; (2) R837/LNP-M-L migrates with lymph flowing into the draining LNs and is taken up by the DCs in the LNs; (3) R837/LNP-M-L triggers maturation of the DCs; (4) the mature DCs present the multi-antigens to the cell surface for naive T cells recognition; (5) the naive T cells differentiate into the CTLs; (6) the CTLs leave from the LNs through the efferent lymphatic vessel; (7) the CTLs recognize and eradicate tumor cells, showing enhanced antitumor efficacy in combination with aPD1; (8) the CTLs can transform into memory T cells; (9) the memory T cells are rapidly converted into large numbers of CTLs upon re-exposure to the specific invading antigens to eliminate tumor cells.

Cou6-tagged LNP-M (Cou6/LNP-M) for 4 hours. The fluorescent intensity of Cou6 within the DCs was quantified by flow cytometry.

For investigation of the influencing factor of the core component, four LNP-M formulated with soybean phosphatidylcholine (SPC), cholesterol, and different additive lipid constituents involving tributyrin (TB), tricaprin (TC), triolein (TO), and cholesteryl oleate (CO) were prepared. The particle sizes of LNP-M were controlled to be similar, approximately 130 nm. No statistical difference in the fluorescent intensities of DiD in the skin-draining LNs of the mice receiving four kinds of DiD/LNP-M (Fig. 2, A and B), indicating that the studied composition of lipid core has no notable effect on the in vivo LN-targeted capacity of LNP-M. However, Cou6/LNP-M with different lipid cores exhibited an obvious difference in the DC uptake. LNP-M containing TO or CO with long-chain alkanes significantly increased intracellular accumulation as evidenced by higher fluorescent intensity of Cou6 within the DCs (Fig. 2C), which is because the DCs preferentially internalize foreign structures with stronger hydrophobic cores and longer alkyl chains (*43*). Moreover, the melting point of CO

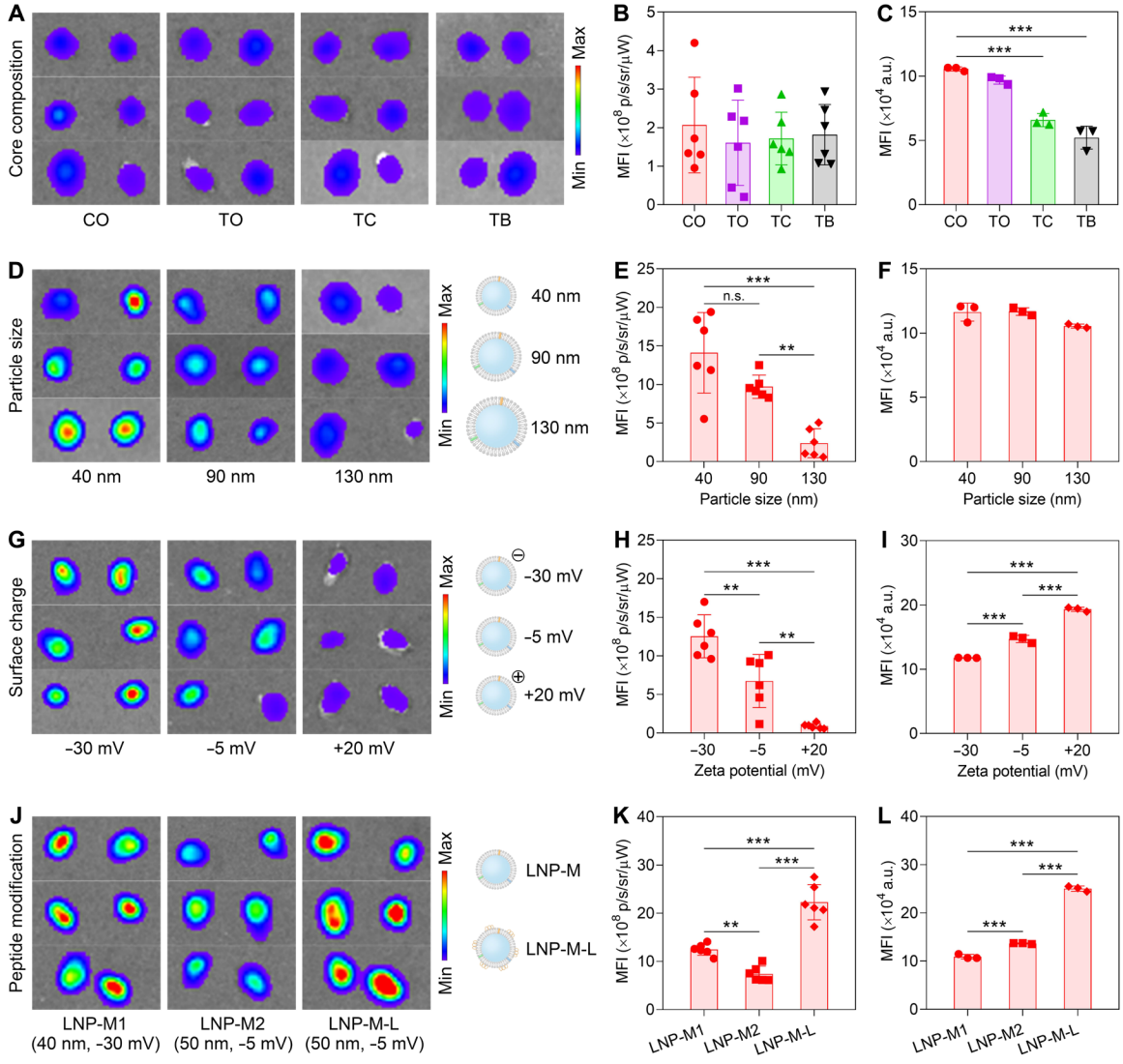

Fig. 2. Evaluation of nanoparticulate property for lymphatic targeting and DC uptake. (**A** and **B**) Ex vivo fluorescence imaging (A) and fluorescent intensities (B) of the LNs harvested from the mice at 24 hours after inoculation of DiD/LNP-M with different core compositions ($n = 3$ mice per group). MFI: mean fluorescent intensity. (**C**) Fluorescent intensities of the DCs at 4 hours after incubation with Cou6/LNP-M with different core compositions ($n = 3$). (**D** and **E**) Ex vivo fluorescence imaging (D) and fluorescent intensities (E) of the LNs at 24 hours after inoculation of DiD/LNP-M with different particle sizes ($n = 3$ mice per group). (**F**) Fluorescent intensities of the DCs at 4 hours after incubation with Cou6/LNP-M with different particle sizes. (**G** and **H**) Ex vivo fluorescence imaging (G) and fluorescent intensities (H) of the LNs at 24 hours after inoculation of DiD/LNP-M with different surface charges ($n = 3$ mice per group). (**I**) Fluorescent intensities of the DCs at 4 hours after incubation with Cou6/LNP-M with different particle sizes ($n = 3$). (**J** and **K**) Ex vivo fluorescence imaging (J) and fluorescent intensities (K) of the LNs at 24 hours after subcutaneous inoculation of DiD/LNP-M1 (40 nm, −30 mV), DiD/LNP-M2 (50 nm, −5 mV), or DiD/LNP-M-L (50 nm, −5 mV) ($n = 3$ mice per group). (**L**) Fluorescent intensities of the DCs at 4 hours after incubation with Cou6/LNP-M1 (40 nm, −30 mV), Cou6/LNP-M2 (50 nm, −5 mV), or Cou6/LNP-M-L (50 nm, −5 mV) ($n = 3$). Data are shown as means ± SD [(B), (C), (E), (F), (H), (I), (K), and (L)]. Statistical significance was determined by one-way analysis of variance (ANOVA) with a Tukey post hoc test [(C), (E), (H), (I), (K), and (L)]. $P > 0.05$ (no significance, n.s.), $^{**}P < 0.01$, and $^{***}P < 0.001$.

(~50°C) is above body temperature and much higher than that of TO (~0°C) (*44*), suggesting that the CO-containing LNP-M has preferable stability. Together, LNP-M with CO-formed lipid core was selected for further studies in consideration of high stability, appreciable lymphatic targeting, and favorable DC uptake.

Next, to evaluate the effect of particle size on the lymphatic targeting and DC uptake of LNP-M, we prepared three LNP-M with similar surface charge (−30 mV) but different particle sizes (40, 90, and 130 nm). LNP-M showed increased accumulation in the LNs as the particle size decreased (Fig. 2, D and E). The DiD fluorescent intensity in the LNs of the 40-nm-sized LNP-M–treated group was 1.5- and 5.9-fold that of the 90-nm- and 130-nm-sized LNP-M–treated groups, respectively. By comparison, the particle size had no substantial effect on the DC uptake of LNP-M at the studied size range (Fig. 2F). Furthermore, the surface charge impact was estimated. Three LNP-M with comparable particle size (40 nm) but different surface charges (−30, −5, and +20 mV) were obtained by incorporation of cetyltrimethylammonium bromide at different amounts. Highly negatively charged LNP-M exhibited superior LN-targeted capacity than its positively charged counterpart (Fig. 2, G and H). In sharp contrast, positive surface charge promoted the DC uptake of LNP-M (Fig. 2I), which is mainly attributed to increased adsorption of LNP-M on the negatively charged cell membrane of the DCs by electrostatic interaction. The results indicate that small particle size and negative surface charge facilitate the lymphatic drainage of LNP-M, while positive surface charge increases the DC uptake of LNP-M.

We further assessed the effect of surface modification of the 22A peptide on the LN accumulation and DC uptake of LNP-M. LNP-M-L was prepared by hydrophobic and electrostatic interactions between the membrane lipid biolayer and the 22A peptide. The positive charge and hydrophobic amino acid segment enabled the 22A peptide to be absorbed and anchored on the negatively charged membrane lipid biolayer of LNP-M. The obtained LNP-M-L had an increased particle size and a decreased negative charge compared with the undecorated LNP-M (fig. S1). We first compared the in vivo lymphatic targeting efficiency of LNP-M-L with LNP-M which had the same particle size and surface charge. Prominently higher lymph-targeting efficiency of LNP-M-L was determined, as substantiated by significant elevation of the DiD fluorescent intensity within the harvested LNs (Fig. 2, J and K), suggesting that surface functionalization of the 22A peptide promotes the nanoparticle to penetrate the lymphatic vessels via active transmembrane transport mediated by the SR-BI receptor expressed on lymphatic endothelial cells, resulting in enhanced accumulation in the LNs. Notably, LNP-M-L with mild negative charge showed significantly increased accumulation in the LNs than the unmodified LNP-M with a high negative charge and smaller particle size, further reflecting that the SR-BI–mediated active permeation through the lymphatic vessel wall plays a dominant role in enhancing the LN-targeted capability of LNP-M-L compared with the passive diffusion. Encouragingly, LNP-M-L presented significantly higher uptake by the DCs than both control LNP-M (Fig. 2L), and by the SR-BI-expressing human B cell lymphoma (Ramos) cells than by the human T lymphocyte (Jurkat) cells without SR-BI expression (fig. S2), indicating that the peptide modification also promotes the DC uptake of the nanoparticles.

In addition to lymphatic drainage, the retention of nanoparticle-based vaccine in the LNs is also one of the major requisites for effective cell interaction and antigen presentation (*19*). We monitored the biodistribution of DiD/LNP-M-L by IVIS within a long period of 96 hours after subcutaneous injection in the mice at the tail base (Fig. 3A). As expected, both DiD/LNP-L and DiD/LNP-M-L exhibited superior capacity to rapidly transport to the skin-draining LNs than either DiD/LNP or DiD/LNP-M. A stronger fluorescent signal of DiD was detected in the LNs 2 hours after injection of DiD/LNP-M-L. More significantly, DiD/LNP-M-L showed higher LN retention ability than DiD/LNP-M (fig. S3). At 96 hours after injection, the LNs and major tissues including the heart, liver, spleen, lung, and kidney were immediately harvested from the mice, followed by ex vivo fluorescence imaging and region-of-interest (ROI) quantitative analysis (Fig. 3, B and C). The fluorescent signal of DiD in the LNs of the mice was obviously higher than that in other normal tissues. Moreover, the DiD fluorescent signal within the LNs of the mice after treatment with DiD/LNP-M-L was noticeably stronger than that treated with DiD/LNP-M. The fluorescent intensity in the LNs of the DiD/LNP-M-L–treated group was about 2.1-fold that of the DiD/LNP-M–treated group. The harvested LNs were subsequently sliced by freezing microtomy, followed by confocal microscopic observation (Fig. 3, D and E). A notably high fluorescent signal of DiD was visualized and determined in the LNs of the DiD/LNP-M-L–treated group.

Preparation and characterization of R837/LNP-M-L

R837/LNP-M was prepared by coating the cancer cell membrane onto the surface of R837/LNP through repeated extrusion. The 22A peptide was anchored on R837/LNP-M to obtain R837/LNP-M-L. Upon the formulation optimization, the obtained R837/LNP-M-L had the encapsulation efficiency of 93.94% and drug loading of 0.84% (fig. S4). The mass ratio of membrane protein content to R837 was approximately 1.1:1. The particle size increased from 25 nm of R837/LNP to 39 nm of R837/LNP-M and 51 nm of R837/LNP-M-L, and the zeta potential changed from −30 mV of R837/LNP to −29 mV of R837/LNP-M and −5 mV of R837/LNP-M-L (Fig. 4A). The transmission electron microscopy (TEM) images exhibited the spherical morphologies of R837/LNP, R837/LNP-M, and R837/LNP-M-L (fig. S5). The SDS–polyacrylamide gel electrophoresis (SDS-PAGE) analysis displayed that the distribution pattern of protein bands of R837/LNP-M-L was consistent with that of the pure cell membranes (*45*), and the 22A peptide was successfully modified on R837/LNP-M-L (Fig. 4B). R837/LNP-M-L had a high stability (fig. S6).

The release behavior of R837 from R837/LNP-M-L was determined (Fig. 4C). R837/LNP-M-L exhibited a sustained release of R837. Of note, the release rate of R837 under acidic conditions was faster than that under neutral conditions. About 11% of R837 was released from R837/LNP-M-L at pH 7.4, while 22% was released at pH 5.5, a level comparable to the endosomal pH value in the first 1 hour. R837/LNP-M-L released 46% of R837 at pH 7.4, but 90% at pH 5.5 within 48 hours. This is because the protonation of aromatic amines in the structure of R837 under acidic conditions accelerates its release from R837/LNP-M-L (*46*). The results indicate that R837 can be rapidly released in the acidic environment of endosomes within the DCs for efficient activation of TLR7/8 in the endosomes to potentiate immune responses.

Next, we investigated the uptake of the nanoparticles by the DCs in vitro. The DCs were incubated with different Cou6-loaded nanoparticles for 4 hours and were analyzed by flow cytometry (Fig. 4D). There is no marked difference in the Cou6 fluorescent intensities between the Cou6/LNP and Cou6/LNP-M groups, suggesting that the cell membrane coating does not influence the DC uptake

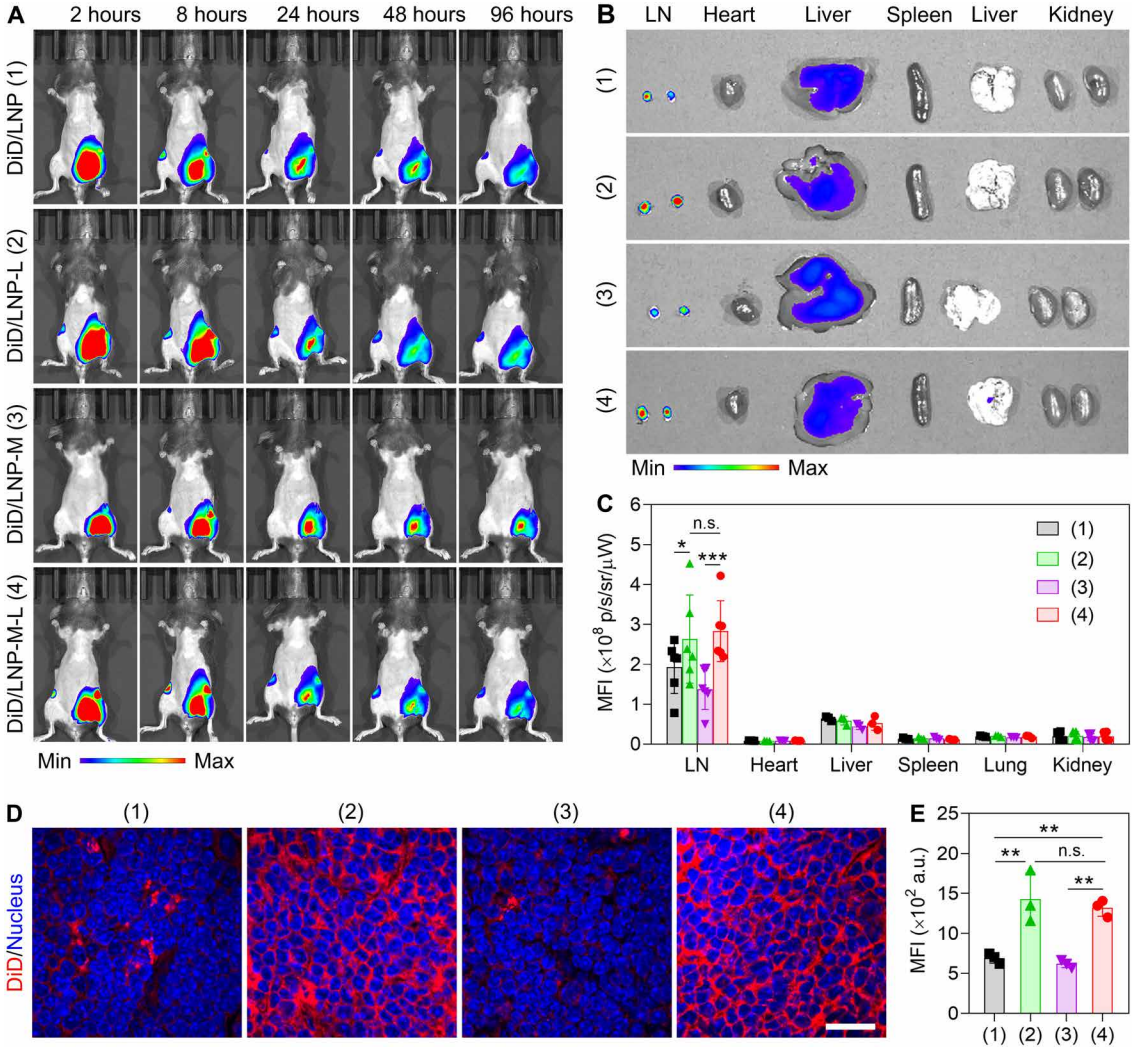

Fig. 3. Validation of enhanced retention of LNP-M-L in the LNs. (**A**) In vivo fluorescence imaging of the mice at different time after inoculation of different DiD-loaded nanoparticles. (**B** and **C**) Ex vivo fluorescence imaging (B) and fluorescent intensities (C) of different tissues harvested from the mice at 96 hours after inoculation of different DiD-loaded nanoparticles. (**D** and **E**) Confocal microscopic imaging (D) and fluorescent intensities (E) of the LNs harvested from the mice at 96 hours after inoculation of different DiD-loaded nanoparticles. Scale bar, 20 μm. The nuclei were stained by 4′,6-diamidino-2-phenylindole. Data are shown as means ± SD [(C) and (E)]. Statistical significance was determined by two-way ANOVA with a Tukey post hoc test (C) or by one-way ANOVA with a Tukey post hoc test (E). $P > 0.05$ (n.s.), $^{*}P < 0.05$, $^{**}P < 0.01$, and $^{***}P < 0.001$.

of LNP. As expected, the fluorescent intensity of Cou6 in the DCs treated with Cou6/LNP-M-L was significantly higher than that treated with either Cou6/LNP or Cou6/LNP-M, indicating that the surface modification of the 22A peptide promotes the uptake of LNP by the SR-BI–expressing DCs (*47*).

The activation of DCs by R837/LNP-M-L was further evaluated by monitoring specific surface biomarker expression (Fig. 4, E to G). The DCs were incubated with different nanoparticles for 24 hours, and the expression of costimulatory molecules including CD40, CD80, and CD86 on the DCs were analyzed by flow cytometry. The blank LNP or LNP-L did not show any effect on the studied surface biomolecules of the DCs. By comparison, both R837/LNP–and LNP-M–treated DCs presented an elevation of expression of all three biomolecules. Significant up-regulation was determined after treatment with R837/LNP-M, suggesting that R837/LNP-M–mediated co-delivery of the antigen-expressing cancer cell membrane with the immune adjuvant displayed considerable effect on forcing activation of the DCs. The R837/LNP-M-L treatment brought about significantly higher levels of CD40, CD80, and CD86 expressions on the DCs in comparison with the R837/LNP-M treatment, confirming that the increased uptake of R837/LNP-M-L markedly boosts the DC activation. In addition, R837/LNP-M-L did not show any obvious cytotoxicities toward the DCs and the murine monocyte/macrophage (RAW264.7) cells within the studied concentrations (fig. S7).

We further evaluated the lymphatic migration and retention of R837/LNP-M-L in vivo. The mice subcutaneously injected with the DiD and R837 co-loaded LNP-M-L (DiD/R837/LNP-M-L) at the tail base were monitored by IVIS (Fig. 4H). DiD/R837/LNP-M-L retained favorable accumulation and retention in the LNs comparable to DiD/LNP-M-L. A high fluorescent signal of DiD was determined in the

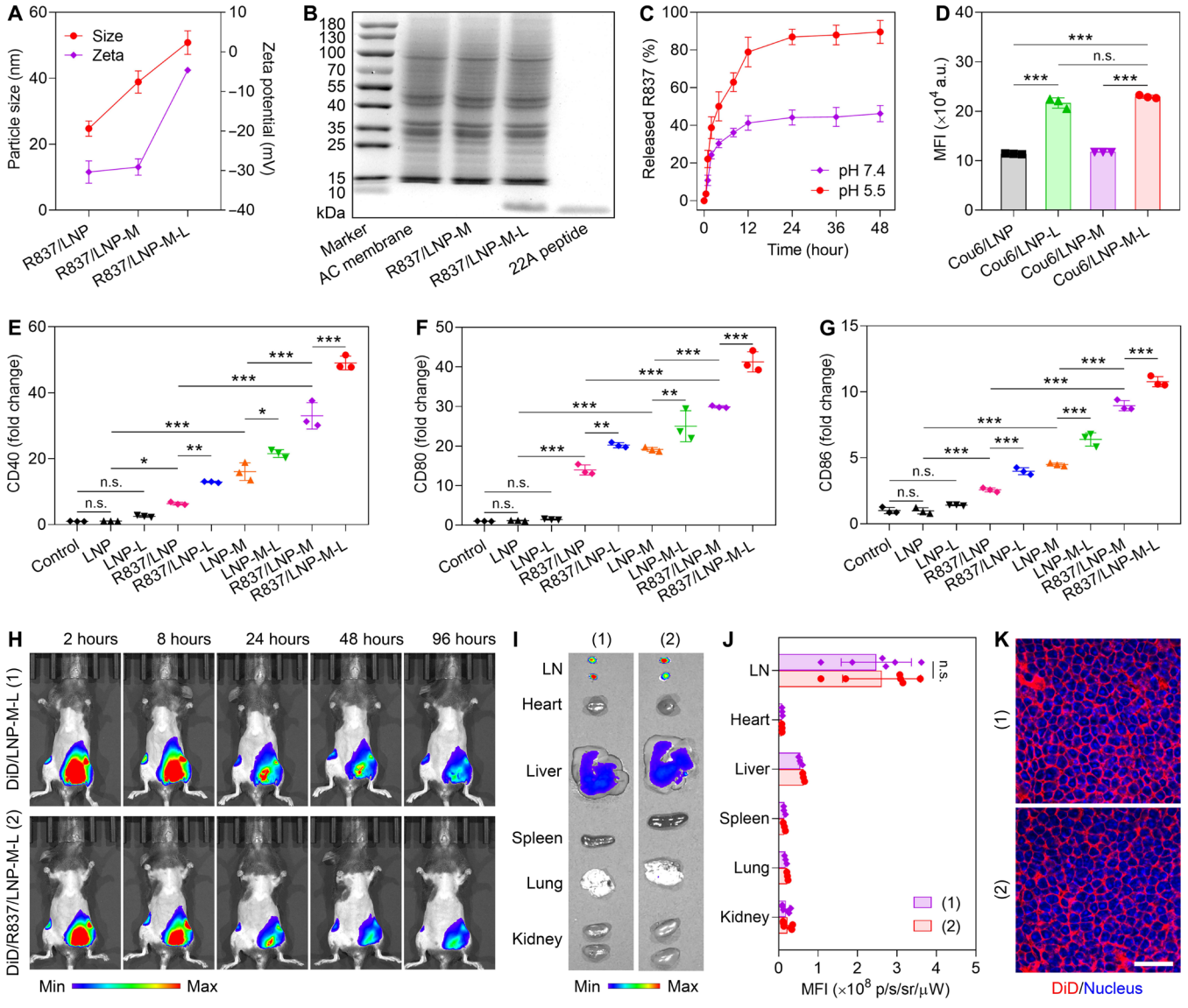

Fig. 4. Construction and characterization of R837/LNP-M-L. (**A**) Particle sizes and zeta potentials of different R837-loaded nanoparticles ($n = 3$). (**B**) SDS–polyacrylamide gel electrophoresis analysis of the proteins from the B16F10 AC membrane, R837/LNP-M, R837/LNP-M-L, and the 22A peptide. (**C**) Release profiles of R837 from R837/LNP-M-L at pH 7.4 and pH 5.5 ($n = 3$). (**D**) Fluorescent intensities of the DCs at 6 hours after incubation with different Cou6-loaded nanoparticles ($n = 3$). (**E** to **G**) Flow cytometric quantification of relative expression of CD40 (E), CD80 (F), and CD86 (G) on the DCs at 24 hours after incubation with different nanoparticles ($n = 3$). (**H**) In vivo fluorescence imaging of the mice at different time after inoculation of DiD/LNP-M-L and DiD/R837/LNP-M-L. (**I** and **J**) Ex vivo fluorescence imaging (I) and fluorescent intensities (J) of different tissues harvested from the mice at 96 hours after inoculation of DiD/LNP-M-L and DiD/R837/LNP-M-L. (**K**) Confocal microscopic imaging of the LN sections at 96 hours after inoculation of DiD/LNP-M-L and DiD/R837/LNP-M-L. Scale bar, 20 μm. Data are shown as means ± SD [(A), (C) to (G), and (J)]. Statistical significance was determined by one-way ANOVA with a Tukey post hoc test [(D) to (G)] or by two-way ANOVA with a Tukey post hoc test (J). $P > 0.05$ (n.s.), $^{*}P < 0.05$, $^{**}P < 0.01$, and $^{***}P < 0.001$.

LNs of the mice in the first 2 hours and remained within 96 hours after injection of DiD/R837/LNP-M-L (fig. S8). The ex vivo imaging and ROI quantification results showed that the DiD fluorescent intensity was markedly higher in the harvested LNs than in other tissues at 96 hours after injection (Fig. 4, I and J). The DiD fluorescent intensities of the LNs presented no significant difference between the DiD/LNP-M-L and DiD/R837/LNP-M-L groups (Fig. 4K and fig. S9). In addition, the LN section was examined by immunofluorescent staining. The DiD fluorescent signal of DiD/LNP-M-L was highly overlapped with that of the DCs (fig. S10), indicating that most of the infiltrating R837/LNP-M-L target the DCs in the LNs. Collectively, the encapsulation of R837 does not affect the lymphatic-targeting property of LNP-M-L. R837/LNP-M-L supports efficient co-delivery of antigens and adjuvants to the DCs in the LNs, which lays a vital foundation for the activation of the anticancer immune response.

Prophylactic effects of R837/LNP-M-L on inhibiting tumor formation

The in vivo antitumor effects of R837/LNP-M-L were first estimated on the prophylactic model of melanoma (*48*). The mice were

subcutaneously immunized with different LNP-based vaccines, including R837/LNP-L, R837/LNP-M, LNP-M-L, and R837/LNP-M-L at the tail base three times with an interval of 1 week. At 7 days after the last immunization, the mice were challenged by subcutaneous implantation of the B16F10 ACs, and the tumor formation and growth were monitored (fig. S11A). Vaccination with R837/LNP-M-L showed the highest effects on delaying tumor formation, as embodied by the slowest speed of tumor generation and the lowest volume of the formed tumor (fig. S11, B to E).

Next, we evaluated the prophylactic efficacy of R837/LNP-M-L in inhibiting the formation and development of high-stemness melanoma. The B16F10 ACs were cultured under serum-free suspension conditions and formed tumorspheres with enrichment of CSC population (*49*), as characterized by up-regulated expression of ABCB5, a specific stemness-related surface biomarker and Nanog, a typical stemness-associated transcription factor (fig. S12). As examined by the SDS-PAGE analysis, the cell membrane protein expression of the tumorsphere cells (TCs) was notably different from that of the ACs, including protein types and contents (Fig. 4B and fig. S13). The cell membranes of the TCs were used for the preparation of R837/LNP-M-L. The obtained R837/LNP-M-L preserved the protein expression on the cell membranes of the TCs (fig. S13). After immunization, the mice were challenged by the B16F10 TCs (Fig. 5A). The CSC-enriched B16F10 TCs showed higher in vivo tumorigenic ability than the ACs. Only 40% of the saline-treated mice developed tumors at 13 days after inoculation of the ACs (fig. S11D), while all the mice generated tumors within 12 days after implantation of the TCs at even low inoculated cell density (fig. S14). R837/LNP-M-L exhibited a potent effect on retarding tumor formation and inhibiting tumor growth (Fig. 5, B and C, and fig. S14). The tumor size of the R837/LNP-M-L–immunized mice was significantly smaller than that of other treated mice at 22 days after inoculation of the TCs (Fig. 5D). The mice immunized with R837/LNP-M-L had markedly prolonged survival period (Fig. 5E). No noticeable change of the mouse body weight was found after treatment with R837/LNP-M-L (fig. S15). These results indicate that R837/LNP-M-L acts as an efficacious cancer vaccine to suppress the melanoma occurrence and progression, and moreover, fulfills personalized immunization against melanoma with different malignant degrees including high-stemness counterpart by being equipped with cytomembrane of melanoma cells with distinct phenotypes.

To investigate the mechanism behind the noticeable prophylactic efficacy of R837/LNP-M-L against the challenge of the B16F10 TCs, we evaluated the protective immune response of mice after vaccination. Both LNs and spleens were harvested from the mice 7 days after the last vaccination. The proportions of the memory T cells in the tissues were analyzed by flow cytometry. Immunization with R837/LNP-M-L resulted in prominent elevation of the ratios of memory T cells in the LNs, including the $CD8^+$ central memory T (T_{cm}) cells ($CD3^+CD8^+CD44^+CD62L^+$), the $CD8^+$ effector memory T (T_{em}) cells ($CD3^+CD8^+CD44^+CD62L^-$), the $CD4^+$ T_{cm} cells ($CD3^+CD4^+CD44^+CD62L^+$), and the $CD4^+$ T_{em} cells ($CD3^+CD4^+CD44^+CD62L^-$) (Fig. 5, F to I, and fig. S16). The proportions of the $CD8^+$ T_{cm}, $CD8^+$ T_{em}, $CD4^+$ T_{cm}, and $CD4^+$ T_{em} cell population in the R837/LNP-M-L–treated group were 6.9-, 4.1-, 3.6-, and 4.8-fold that in the saline-treated group, respectively. Both $CD8^+$ and $CD4^+$ T_{em} cell populations in the spleens of the mice immunized with R837/LNP-M-L were also significantly higher than that of the mice vaccinated with other LNPs (Fig. 5, J and K, and fig. S17). After treatment with R837/LNP-M-L, the ratios of $CD8^+$ and $CD4^+$ T_{em} cells in the spleens were 2.6- and 1.9-fold that after treatment with saline. Accordingly, R837/LNP-M-L elicits and maintains protective cellular immunity reflected by elevation of the $CD8^+$ T_{cm} and T_{em} cell frequency in the immune organs such as the LN and spleen to promptly supply the effector $CD8^+$ T cells and elicit CTL response against tumor formation. Promotion of the $CD4^+$ T_{cm} and T_{em} cell proportion produced by R837/LNP-M-L also facilitates the increase of tumor infiltration of the helper $CD4^+$ T cells for further augmenting the CTL response.

Therapeutic effects of R837/LNP-M-L on inhibiting tumor growth

With the confirmation of the enhanced effectiveness of R837/LNP-M-L on inhibiting tumor formation and growth by providing long-term immune surveillance and protection, we explored whether R837/LNP-M-L could serve as a therapeutic cancer vaccine to induce tumor regression and assessed the combination anticancer efficacy of R837/LNP-M-L with the clinically applied immune checkpoint inhibitor, anti-PD1 antibody (aPD1). After subcutaneous implantation of the B16F10 TCs, the mice were subcutaneously immunized with R837/LNP-M-L, intravenously injected with aPD1 and combination of R837/LNP-M-L and aPD1, respectively, and the tumor growth was monitored (Fig. 6A). Treatment with aPD1 produced limited tumor inhibitory effect (Fig. 6B), which is mainly attributed to tumor stemness-derived innate immunoresistance and immunosuppressive microenvironment. By comparison, vaccination with R837/LNP-M-L generated preferable suppression of tumor growth. The R837/LNP-M-L immunization markedly augmented the therapeutic efficacy of aPD1 on tumor inhibition. Combined utilization of R837/LNP-M-L and aPD1 (R837/LNP-M-L + aPD1) had a significantly stronger inhibitory effect on tumor development than the application of R837/LNP-M-L or aPD1 alone. The lowest tumor size of the mice receiving combinatorial treatment was achieved (Fig. 6C). Combination treatment did not cause any evident variations of the mouse body weight (Fig. 6D). The histological examination using hematoxylin and eosin (H&E) staining showed that treatment with R837/LNP-M-L + aPD1 led to extensive cell death in the tumor tissue (fig. S18A) but did not cause any observable pathological abnormalities in the normal tissues such as the heart, liver, spleen, lung, and kidney (fig. S18B). Expression of stemness-related biomolecules including Nanog, Sox2, and ABCB5 within the tumors was further inspected using immunohistochemical and immunofluorescent staining (figs. S19 and S20). Compared with the aPD1-treated group, significant down-regulation of the biomolecule expression was found in the R837/LNP-M-L–treated group. A combination of R837/LNP-M-L with aPD1 distinctly reduced intratumoral expression of all three stemness-associated biomolecules. Furthermore, the jointly treated mice had a longer survival period than the mono-treated ones (Fig. 6E). These findings indicate that R837/LNP-M-L serves as a therapeutic vaccine to potentiate the antitumor efficacy of aPD1-mediated immunotherapy against the CSC-enriched resistant melanoma. In addition, the treatment does not induce any conspicuous variation in serum levels of liver and kidney biochemical indices, such as alanine aminotransferase, aspartate aminotransferase, creatinine, and blood urea nitrogen (fig. S21).

To further explore the underlying mechanisms of the constructed R837/LNP-M-L against tumor progression, the tumors and LNs were harvested from the mice at 22 days after different treatments, followed by flow cytometric analysis of immune cell infiltration (Fig. 6, F to K).

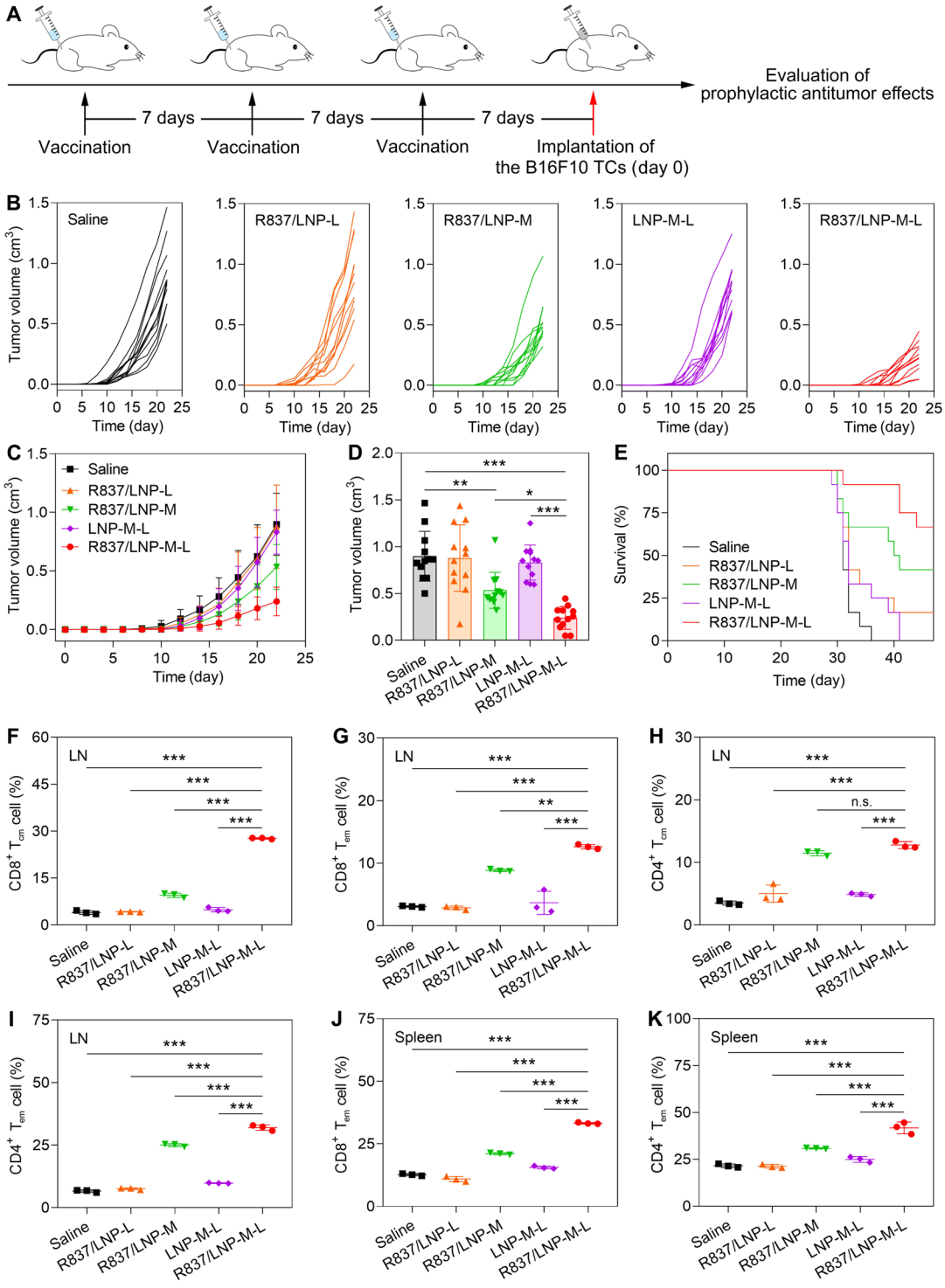

Fig. 5. Prophylactic antitumor effects of R837/LNP-M-L on the CSC-enriched melanoma mouse model. (**A**) Schematic illustration to evaluate the prophylactic antitumor effects after different treatments. (**B** and **C**) Changes in individual (B) and average (C) tumor volumes of the mice after different treatments ($n = 12$ mice per group). (**D**) Tumor volumes of the mice at 22 days after implantation of the B16F10 TCs ($n = 12$ mice per group). (**E**) Survival curves of the mice after different treatments ($n = 12$ mice per group). (**F** to **K**) Percentages of the $CD8^+$ T_{cm} (F), $CD8^+$ T_{em} (G), $CD4^+$ T_{cm} (H), and $CD4^+$ T_{em} (I) cells in the LNs and the $CD8^+$ T_{em} (J) and $CD4^+$ T_{em} (K) cells in the spleens harvested from the mice at 22 days after first inoculation of different nanoparticles ($n = 3$ mice per group). Data are shown as means ± SD [(C), (D), and (F) to (K)]. Statistical significance was determined by one-way ANOVA with a Tukey post hoc test [(D) and (F) to (K)]. $P > 0.05$ (n.s.), $^*P < 0.05$, $^{**}P < 0.01$, and $^{***}P < 0.001$.

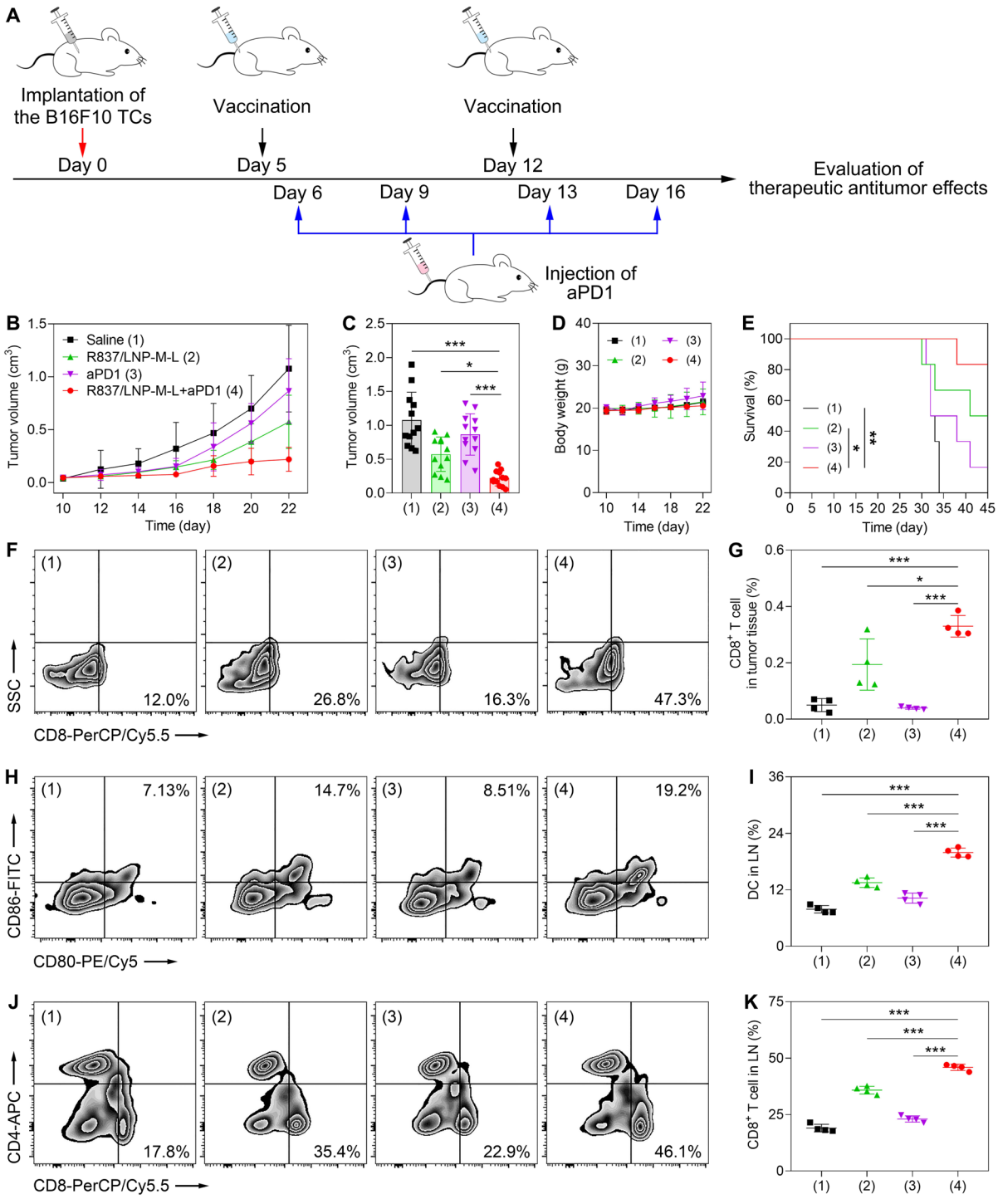

Fig. 6. Therapeutic antitumor effects of R837/LNP-M-L on the CSC-enriched melanoma mouse model. (**A**) Schematic illustration to evaluate the therapeutic antitumor effects after different treatments. (**B**) Tumor growth profiles of the mice after different treatments ($n = 12$ mice per group). (**C**) Tumor volumes of the mice at 22 days after implantation of the B16F10 TCs after different treatments ($n = 12$ mice per group). (**D** and **E**) Body weight changes (D) and survival curves (E) of the mice after different treatments ($n = 12$ mice per group). (**F** to **K**) Flow cytometric images and quantification of the $CD8^+$ T cells in the tumors [(F) and (G)], the DCs [(H) and (I)], and $CD8^+$ T cells in the LNs [(J) and (K)] harvested from the mice at 22 days after implantation of the B16F10 TCs after different treatments ($n = 4$). Data are shown as means ± SD [(B) to (C), (G), (I), and (K)]. Statistical significance was determined by one-way ANOVA with a Tukey post hoc test [(C), (G), (I), and (K)] or by a two-sided log-rank (Mantel-Cox) test (E). $^*P < 0.05$, $^{**}P < 0.01$, and $^{***}P < 0.001$.

The tumor of the mice treated with R837/LNP-M-L displayed significant elevation of the $CD8^+$ cell infiltration, while no marked increase of the $CD8^+$ cell ($CD45^+CD3^+CD8^+$) percentage was determined in the tumors after the aPD1 treatment. The proportion of the $CD8^+$ cells within the R837/LNP-M-L–treated tumor was 3.9-fold that of the saline-treated tumor. Notably, a combination of R837/LNP-M-L and aPD1 resulted in substantial promotion of the $CD8^+$ cell infiltration. The infiltrating $CD8^+$ T cell percentage was 1.7- and 6.6-fold that of the saline and R837/LNP-M-L groups, respectively. Meanwhile, the R837/LNP-M-L vaccination promoted the infiltration of both DCs and $CD8^+$ T cells into the LNs. Moreover, the immune cell infiltration was significantly enhanced in combination with aPD1. The proportions of the DCs and $CD8^+$ cells in the LNs after combinatorial treatment were 2.6- and 2.3-fold that after the saline treatment, respectively. These data suggest that vaccination with R837/LNP-M-L overcomes the tumor immunosuppressive microenvironment and elicits effective immune responses as evidenced by increased frequency of the $CD8^+$ T cells within both tumors and LNs, which brings about enhanced therapeutic efficacy in combination with aPD1.

DISCUSSION

We have developed an HDL-mimetic LNP-based cancer nanovaccine having a high lymph-targeted potency, which is packed with tumor-specific membrane antigens and encapsulated with R837 adjuvant, for personalized cancer immunotherapy. We explore and reveal the relationship between the nanoparticle properties and the lymphatic targeting capacity, as well as the DC uptake efficiency. The core composition does not affect the LN-targeted efficiency of LNP-M, but the LNP-M containing the hydrophobic core formed by longer alkyl chain lipids is more likely to be taken up by the DCs. Small particle size and negative charge promote the subcutaneously injected LNP-M to migrate to the LNs (*35*). However, the particle size does not affect the DC uptake within the size range investigated, while the positive charge increases the DC uptake. Of note, the surface modification with the 22A peptide boosts both LN accumulation and DC uptake despite increased particle size and neutralized surface charge, indicating that active transport plays a significant role in enhancing the permeation of the nanoparticle into the lymphatic vessels and eventually increasing accumulation in the LNs. Upon optimization, the obtained LNP-M-L not only shows more lymphatic transportation but also prolongs retention accompanied by elevated DC uptake within the draining LNs.

On the basis of the optimized formulation, R837 is efficiently loaded in the hydrophobic core, and the antigen-expressing cancer cell membrane is engineered on the surface on demand. R837/LNP-M-L exhibits sustained release of R837, and the release rate accelerates under acidic conditions, rendering promotion of the TLR7/8 activation of R837 within the acidic endocytic vesicles of the DCs. R837LNP-M-L shows a potent effect on hastening the activation and maturation of the DCs by co-delivery of R837 and tumor antigens, and promoting elevation of the $CD8^+$ T cell proliferation and infiltration, resulting in delay of tumor formation in the prophylactic mouse model of melanoma.

Identification of antigens that can elicit antitumor immunity is of vital importance to cancer vaccines. We find out that the expression patterns of membrane protein are noticeably different between the ACs and the CSC-enriched TCs, suggesting that personalized development of a cancer vaccine that is directed against CSCs is essential for the treatment of high-stemness tumors with high tumorigenicity. To this end, the cytomembrane of the TCs is formulated in R837/LNP-M-L. We demonstrate that the obtained R837/LNP-M-L can act as a combined prophylactic and therapeutic cancer nanovaccine. Investigated on the prophylactic mouse model of CSC-enriched melanoma, vaccination of R837/LNP-M-L evokes strong immune responses, as manifested by increased frequency of the $CD8^+$ and $CD4^+$ T_{em} cell populations in the LNs and spleens, to significantly decrease the tumor formation rate and retards the tumor progression. Of note, the CSC-enriched melanoma is found to be highly resistant to aPD1-mediated therapy. Immunization of R837/LNP-M-L sensitizes the high-stemness melanoma to aPD1 and augments the therapeutic effect of aPD1. The proportions of the activated DCs in the LNs and the $CD8^+$ T cells in the LNs and tumors are noticeably elevated after treatment with R837/LNP-M-L, confirming that R837/LNP-M-L can elicit efficient cellular immunity to fight tumors with high stemness.

At last, all the components used for the formulation are approved by the FDA. Safety investigations show that R837/LNP-M-L does not cause any observable liver and kidney function impairment and pathological tissue changes within the studied period. For further clinical translation, a long-term safety assessment of the formulation should be carried out. Moreover, additional studies for further validation of efficacy will be necessary to perform on large animal models.

MATERIALS AND METHODS

Preparation and characterization of R837/LNP-M-L

LNP was prepared using the nanoprecipitation method. Briefly, 8 ml of acetone dissolving CO, TO, TC, or TB (6 mg) and cholesterol (3 mg) was mixed with 2 ml of ethanol dissolving SPC (60 mg). The organic solution was dripped slowly into 30 ml of Tris-HCl buffer [10 mM Tris, 0.1 M KCl, and 1 mM EDTA (pH 8)] containing sodium cholate (30 mg) under stirring at 1000 rpm. After continuous stirring for 2 hours, the suspension was dispersed by ultrasonication. The organic solvent was removed by evaporation under reduced pressure. Subsequently, the suspension was dialyzed against the Tris-HCl buffer [10 mM Tris, 0.1 M KCl, and 1 mM EDTA (pH 8)] at 4°C for 12 hours. The resulting LNP was attained after passing through a 220-nm filter membrane. LNP-M was obtained by co-extruding LNP and cell membranes repeatedly by a mini extruder (LF-1, Avestin). For the preparation of LNP-M-L, LNP-M was incubated with the 22A peptide at 37°C for 8 hours, and the excessive 22A peptide was removed by ultrafiltration. For the modulation of nanoparticulate property, ultrasonic dispersing was used to adjust the particle size, while cetyltrimethylammonium bromide, a cationic surfactant, was applied to modulate the surface charge. For drug loading, R837 together with the lipid components were dissolved in the organic solution, while for the fluorescent tracking, the fluorescent dye, DiD, or Cou6 was added in the organic solution. The particle size and zeta potential of nanoparticles in phosphate-buffered saline (PBS) were determined by Zetasizer (Nano ZS90, Malvern). The morphology of nanoparticles was visualized by TEM (HT7700, Hitachi). The cell membrane proteins of LNP-M or LNP-M-L were characterized by SDS-PAGE gel electrophoresis. For evaluation of drug release, R837/LNP-M-L was placed in a dialysis bag (3.5-kDa molecular weight cutoff) and immersed in PBS (pH 7.4 or 5.5) containing SDS (0.1%) under stirring at 100 rpm at 37°C. At the arranged time intervals, the release medium was sampled, followed by the replacement of the fresh release medium. The

absorbance of the release medium at 325 nm was measured by a microplate reader (Infinite M1000 Pro, Tecan). For assessment of stability, R837/LNP-M-L was stored at 4°C for 7 days, and the particle size, zeta potential, and encapsulated R837 amount were determined over time.

Animal models

The mice (C57BL/6, female, ~20 g) were purchased from the Comparative Medicine Centre of Yangzhou University. All the mice were treated according to the Guide for Care and Use of Laboratory Animals, approved by the Animal Experimentation Ethics Committee of China Pharmaceutical University. All the mice used in the studies were randomly allocated to each experimental group. No formal blinding was used for outcome assessment.

Determination of lymphatic targeting

The mice were subcutaneously injected with different DiD-labeled nanoparticles [DiD (50 μg/kg)] at the tail base. At the prearranged time intervals, the mice were imaged by IVIS (Spectrum, PerkinElmer). At the indicated time points, the mice were euthanized, and the bilateral inguinal LNs and/or heart, liver, spleen, lung, and kidney were harvested, followed by ex vivo imaging by IVIS. The LNs were sliced by a freezing microtome (CryoStar NX50, Thermo Fisher Scientific). The frozen LN sections were stained with the anti-CD11c antibody, fluorescein isothiocyanate–conjugated anti–immunoglobulin G antibody, and 4′,6-diamidino-2-phenylindole and observed by fluorescence microscope (Ts2R, Nikon). The fluorescent intensity and colocalization were determined by ImageJ software.

In vivo prophylactic efficacy

The mice were subcutaneously inoculated with different drug-loaded LNPs [R837 (1 mg/kg) and membrane protein (1.1 mg/kg)] every 7 days (three injections) at the tail base. At 21 days after inoculation, the mice were euthanized, and the bilateral inguinal LNs and spleens were harvested. The T cells within the LNs and spleens were analyzed by detecting specific surface biomarkers using flow cytometry. In addition, the mice were subcutaneously inoculated with the B16F10 ACs (5×10^5 cells per mouse) or TCs (2×10^5 cells per mouse). The tumor growth, tumor formation rate, body weight, and mouse survival were monitored. The tumor volume was calculated by the formula: $V = L \times W^2 \times 0.5$, where V is the volume of the tumor, while L and W are the length and width of the tumor, respectively.

In vivo therapeutic efficacy

The mice were subcutaneously inoculated with the B16F10 TCs (2×10^5 cells per mouse). Subsequently, the mice were subcutaneously injected with different drug-loaded LNPs [R837 (1 mg/kg) and membrane protein (1.1 mg/kg)] at the tail base and were intravenously injected with aPD1 (1 mg/kg). The tumor growth, body weight, and mouse survival were monitored. At the indicated time points, the mice were euthanized, and the tumors and bilateral inguinal LNs were harvested. The tumors were weighed and histologically examined by the H&E staining. The expressions of Nanog, Sox2, and ABCB5 within the tumors were examined by immunohistochemical and immunofluorescent staining and examined using confocal microscopy, respectively. The T cells within the tumors and LNs as well as the DCs within the LNs were analyzed using flow cytometry. In addition, the blood was sampled. The serum levels of alanine aminotransferase, aspartate aminotransferase, creatinine, and blood urea nitrogen were determined using the corresponding assay kits (Nanjing Jiancheng) according to the manufacturers' protocols. The major normal tissues including the heart, liver, spleen, lung, and kidney were harvested and histologically examined by the H&E staining.

Flow cytometric analysis

The single-cell suspension was obtained by mashing the mashed tissues (LN, spleen, or tumor) in PBS passing through a 70-μm cell strainer (BD Falcon). The spleen cell suspension was further treated by the red blood cell lysis buffer. For analysis of immune cells, the cell suspension was stained by the corresponding fluorescence-conjugated antibodies according to the manufacturers' protocols. The stained cells were analyzed by flow cytometer (CytoFLEX S, Beckman Coulter). For detection of the Nanog and Sox2 expression, the tumor cell suspension was fixed by paraformaldehyde (4%) for 10 min, permeabilized by Triton X-100 (0.1%) for 10 min, and blocked by bovine serum albumin (1%) for 60 min. The cells were stained by the corresponding primary antibodies and fluorescence-labeled secondary antibodies according to the manufacturers' protocols and analyzed using flow cytometry. For detection of the ABCB5 expression, the tumor cell suspension without permeabilization process was directly stained by the corresponding primary antibody and fluorescence-labeled secondary antibody according to the manufacturer's protocol, and analyzed by flow cytometry.

H&E, immunohistochemical, and immunofluorescent staining

The tumor and normal tissues were collected from the mice and fixed by paraformaldehyde (4%). The tissues were then embedded in paraffin and sliced into 5-μm-thick sections. For the H&E staining, the tissue slices were stained by H&E and observed by the microscope. For the immunohistochemical staining, the tumor sections were blocked by serum, stained by the corresponding primary antibodies and horseradish peroxidase–conjugated secondary antibody, and treated with diaminobenzidine according to the manufacturers' protocols. The stained tumor sections were observed by the microscope. For the immunofluorescent staining, the tumor sections were blocked by serum and stained by the corresponding primary antibody and fluorescence-labeled secondary antibody according to the manufacturers' protocols. The stained tumor sections were observed by a confocal laser scanning microscope (FV3000, Olympus).

Statistical analysis

Results were presented as means ± SD. Biological replicates were used in all the experiments unless stated otherwise (n numbers are specified in figure legends). The GraphPad Prism software 8.0 was used for statistical analyses. The statistical tests used for each experiment are detailed in the figure legends. $P < 0.05$ was considered statistically significant ($P > 0.05$, no significance, n.s.; $^*P < 0.05$; $^{**}P < 0.01$; $^{***}P < 0.001$).

Supplementary Materials

This PDF file includes:

Supplementary Materials and Methods
Figs. S1 to S21

REFERENCES AND NOTES

1. J. L. Excler, M. Saville, S. Berkley, J. H. Kim, Vaccine development for emerging infectious diseases. *Nat. Med.* **27**, 591–600 (2021).
2. M. Saxena, S. H. van der Burg, C. J. M. Melief, N. Bhardwaj, Therapeutic cancer vaccines. *Nat. Rev. Cancer* **21**, 360–378 (2021).
3. J. Banchereau, K. Palucka, Cancer vaccines on the move. *Nat. Rev. Clin. Oncol.* **15**, 9–10 (2018).
4. U. Sahin, Ö. Türeci, Personalized vaccines for cancer immunotherapy. *Science* **359**, 1355–1360 (2018).
5. T. Ci, H. Li, G. Chen, Z. Wang, J. Wang, P. Abdou, Y. Tu, G. Dotti, Z. Gu, Cryo-shocked cancer cells for targeted drug delivery and vaccination. *Sci. Adv.* **6**, eabc3013 (2020).
6. T. Enokida, A. Moreira, N. Bhardwaj, Vaccines for immunoprevention of cancer. *J. Clin. Invest.* **131**, e146956 (2021).
7. S. Jhunjhunwala, C. Hammer, L. Delamarre, Antigen presentation in cancer: Insights into tumour immunogenicity and immune evasion. *Nat. Rev. Cancer* **21**, 298–312 (2021).
8. W. S. Bowen, A. K. Svrivastava, L. Batra, H. Barsoumian, H. Shirwan, Current challenges for cancer vaccine adjuvant development. *Expert Rev. Vaccines* **17**, 207–215 (2018).
9. J. Liu, M. Fu, M. Wang, D. Wan, Y. Wei, X. Wei, Cancer vaccines as promising immuno-therapeutics: Platforms and current progress. *J. Hematol. Oncol.* **15**, 28 (2022).
10. B. Farhood, M. Najafi, K. Mortezaee, $CD8^+$ cytotoxic T lymphocytes in cancer immunotherapy: A review. *J. Cell. Physiol.* **234**, 8509–8521 (2019).
11. L. Diao, M. Liu, Rethinking antigen source: Cancer vaccines based on whole tumor cell/tissue lysate or whole tumor cell. *Adv. Sci.* **10**, e2300121 (2023).
12. T. Zhao, Y. Cai, Y. Jiang, X. He, Y. Wei, Y. Yu, X. Tian, Vaccine adjuvants: Mechanisms and platforms. *Signal Transduct. Target. Ther.* **8**, 283 (2023).
13. B. Pulendran, P. S. Arunachalam, D. T. O'Hagan, Emerging concepts in the science of vaccine adjuvants. *Nat. Rev. Drug Discov.* **20**, 454–475 (2021).
14. M. E. Aikins, C. Xu, J. J. Moon, Engineered nanoparticles for cancer vaccination and immunotherapy. *Acc. Chem. Res.* **53**, 2094–2105 (2020).
15. G. A. Roth, V. C. T. M. Picece, B. S. Ou, W. Luo, B. Pulendran, E. A. Appel, Designing spatial and temporal control of vaccine responses. *Nat. Rev. Mater.* **7**, 174–195 (2022).
16. G. Liu, M. Zhu, X. Zhao, G. Nie, Nanotechnology-empowered vaccine delivery for enhancing $CD8^+$ T cells-mediated cellular immunity. *Adv. Drug Deliv. Rev.* **176**, 113889 (2021).
17. R. S. Riley, C. H. June, R. Langer, M. J. Mitchell, Delivery technologies for cancer immunotherapy. *Nat. Rev. Drug Discov.* **18**, 175–196 (2019).
18. Q. Wang, Z. Wang, X. Sun, Q. Jiang, B. Sun, Z. He, S. Zhang, C. Luo, J. Sun, Lymph node-targeting nanovaccines for cancer immunotherapy. *J. Control. Release* **351**, 102–122 (2022).
19. Y. Ding, Z. Li, A. Jaklenec, Q. Hu, Vaccine delivery systems toward lymph nodes. *Adv. Drug Deliv. Rev.* **179**, 113914 (2021).
20. H. J. Pownall, C. Rosales, B. K. Gillard, A. M. Gotto Jr., High-density lipoproteins, reverse cholesterol transport and atherogenesis. *Nat. Rev. Cardiol.* **18**, 712–723 (2021).
21. M. Wang, M. R. Briggs, HDL: The metabolism, function, and therapeutic importance. *Chem. Rev.* **104**, 119–138 (2004).
22. A. Y. Shih, S. G. Sligar, K. Schulten, Maturation of high-density lipoproteins. *J. R. Soc. Interface* **6**, 863–871 (2009).
23. H. Y. Lim, C. H. Thiam, K. P. Yeo, R. Bisoendial, C. S. Hii, K. C. Y. McGrath, K. W. Tan, A. Heather, J. S. J. Alexander, V. Angeli, Lymphatic vessels are essential for the removal of cholesterol from peripheral tissues by SR-BI-mediated transport of HDL. *Cell Metab.* **17**, 671–684 (2013).
24. G. J. Randolph, N. E. Miller, Lymphatic transport of high-density lipoproteins and chylomicrons. *J. Clin. Invest.* **124**, 929–935 (2014).
25. A. G. Lacko, M. Nair, L. Prokai, W. J. McConathy, Prospects and challenges of the development of lipoprotein-based formulations for anti-cancer drugs. *Expert Opin. Drug Deliv.* **4**, 665–675 (2007).
26. X. Ma, Q. Song, X. Gao, Reconstituted high-density lipoproteins: Novel biomimetic nanocarriers for drug delivery. *Acta Pharm. Sin. B* **8**, 51–63 (2018).
27. K. K. Ng, J. F. Lovell, G. Zheng, Lipoprotein-inspired nanoparticles for cancer theranostics. *Acc. Chem. Res.* **44**, 1105–1113 (2011).
28. M. G. Damiano, R. K. Mutharasan, S. Tripathy, K. M. McMahon, C. S. Thaxton, Templated high density lipoprotein nanoparticles as potential therapies and for molecular delivery. *Adv. Drug Deliv. Rev.* **65**, 649–662 (2013).
29. R. Kuai, L. J. Ochyl, K. S. Bahjat, A. Schwendeman, J. J. Moon, Designer vaccine nanodiscs for personalized cancer immunotherapy. *Nat. Mater.* **16**, 489–496 (2017).
30. L. Scheetz, P. Kadiyala, X. Sun, S. Son, A. Hassani Najafabadi, M. Aikins, P. R. Lowenstein, A. Schwendeman, M. G. Castro, J. J. Moon, Synthetic high-density lipoprotein nanodiscs for personalized immunotherapy against gliomas. *Clin. Cancer Res.* **26**, 4369–4380 (2020).
31. K. Rajpoot, Solid lipid nanoparticles: A promising nanomaterial in drug delivery. *Curr. Pharm. Des.* **25**, 3943–3959 (2019).
32. X. Yu, Y. Dai, Y. Zhao, S. Qi, L. Liu, L. Lu, Q. Luo, Z. Zhang, Melittin-lipid nanoparticles target to lymph nodes and elicit a systemic anti-tumor immune response. *Nat. Commun.* **11**, 1110 (2020).
33. D. P. Schrijver, A. de Dreu, S. R. J. Hofstraat, E. Kluza, R. Zwolsman, J. Deckers, T. Anbergen, K. de Bruin, M. M. Trines, E. G. Nugraha, F. Ummels, R. J. Röring, T. J. Beldman, A. J. P. Teunissen, Z. A. Fayad, R. van der Meel, W. J. M. Mulder, Nanoengineering apolipoprotein A1-based immunotherapeutics. *Adv. Ther.* **4**, 2100083 (2021).
34. M. Rajora, L. Ding, M. Valic, W. Jiang, M. Overchuk, J. Chen, G. Zheng, Tailored theranostic apolipoprotein E3 porphyrin-lipid nanoparticles target glioblastoma. *Chem. Sci.* **8**, 5371–5384 (2017).
35. A. Schudel, D. M. Francis, S. N. Thomas, Material design for lymph node drug delivery. *Nat. Rev. Mater.* **4**, 415–428 (2019).
36. S. N. Thomas, A. Schudel, Overcoming transport barriers for interstitial-, lymphatic-, and lymph node-targeted drug delivery. *Curr. Opin. Chem. Eng.* **7**, 65–74 (2015).
37. D. Bayik, J. D. Lathia, Cancer stem cell-immune cell crosstalk in tumour progression. *Nat. Rev. Cancer* **21**, 526–536 (2021).
38. J. A. Clara, C. Monge, Y. Yang, N. Takebe, Targeting signalling pathways and the immune microenvironment of cancer stem cells - a clinical update. *Nat. Rev. Clin. Oncol.* **17**, 204–232 (2020).
39. E. Papadavid, A. J. Stratigos, M. E. Falagas, Imiquimod: An immune response modifier in the treatment of precancerous skin lesions and skin cancer. *Expert Opin. Pharmacother.* **8**, 1743–1755 (2007).
40. S. Bhagchandani, J. A. Johnson, D. J. Irvine, Evolution of Toll-like receptor 7/8 agonist therapeutics and their delivery approaches: From antiviral formulations to vaccine adjuvants. *Adv. Drug Deliv. Rev.* **175**, 113803 (2021).
41. C. B. Rodell, S. P. Arlauckas, M. F. Cuccarese, C. S. Garris, R. Li, M. S. Ahmed, R. H. Kohler, M. J. Pittet, R. Weissleder, TLR7/8-agonist-loaded nanoparticles promote the polarization of tumour-associated macrophages to enhance cancer immunotherapy. *Nat. Biomed. Eng.* **2**, 578–588 (2018).
42. L. Guo, E. E. Morin, M. Yu, L. Mei, M. V. Fawaz, Q. Wang, Y. Yuan, C. G. Zhan, T. J. Standiford, A. Schwendeman, X. A. Li, Replenishing HDL with synthetic HDL has multiple protective effects against sepsis in mice. *Sci. Signal.* **15**, eabl9322 (2022).
43. D. B. Moody, V. Briken, T. Y. Cheng, C. Roura-Mir, M. R. Guy, D. H. Geho, M. L. Tykocinski, G. S. Besra, S. A. Porcelli, Lipid length controls antigen entry into endosomal and nonendosomal pathways for CD1b presentation. *Nat. Immunol.* **3**, 435–442 (2002).
44. C. Dumesnil, L. Vanharanta, X. Prasanna, M. Omrane, M. Carpentier, A. Bhapkar, G. Enkavi, V. T. Salo, I. Vattulainen, E. Ikonen, A. R. Thiam, Cholesterol esters form supercooled lipid droplets whose nucleation is facilitated by triacylglycerols. *Nat. Commun.* **14**, 915 (2023).
45. Y. Chen, S. Zhi, J. Ou, J. Gao, L. Zheng, M. Huang, S. Du, L. Shi, Y. Tu, K. Cheng, Cancer cell membrane-coated nanoparticle co-loaded with photosensitizer and toll-like receptor 7 agonist for the enhancement of combined tumor immunotherapy. *ACS Nano* **17**, 16620–16632 (2023).
46. Q.-V. Le, J. Suh, J. J. Choi, G. T. Park, J. W. Lee, G. Shim, Y.-K. Oh, In situ nanoadjuvant-assembled tumor vaccine for preventing long-term recurrence. *ACS Nano* **13**, 7442–7462 (2019).
47. B. Castella, J. Kopecka, P. Sciancalepore, G. Mandili, M. Foglietta, N. Mitro, D. Caruso, F. Novelli, C. Riganti, M. Massaia, The ATP-binding cassette transporter A1 regulates phosphoantigen release and $V\gamma9V\delta2$ T cell activation by dendritic cells. *Nat. Commun.* **8**, 15663 (2017).
48. R. Yang, J. Xu, L. Xu, X. Sun, Q. Chen, Y. Zhao, R. Peng, Z. Liu, Cancer cell membrane-coated adjuvant nanoparticles with mannose modification for effective anticancer vaccination. *ACS Nano* **12**, 5121–5129 (2018).
49. S. Shen, X. Xu, S. Lin, Y. Zhang, H. Liu, C. Zhang, R. Mo, A nanotherapeutic strategy to overcome chemotherapeutic resistance of cancer stem-like cells. *Nat. Nanotechnol.* **16**, 104–113 (2021).

Acknowledgments: We acknowledge the public platform of the State Key Laboratory of Natural Medicines at China Pharmaceutical University for the use of analytical instrumentation facilities and the public platform of the Pharmaceutical Animal Experimental Center at China Pharmaceutical University for the use of a living imaging system. **Funding:** This work was supported by the National Natural Science Foundation of China (82273876, 81971730, and 81673381), the Fok Ying-Tong Education Foundation for Young Teachers in the Higher Education Institutions of China (171028), the Project of State Key Laboratory of Natural Medicines of China Pharmaceutical University (SKLNMZZ202024), and the Project of Jiangsu Key Laboratory of Drug Design and Optimization. **Author contributions:** R.M. conceived and supervised the project. M.L., Y.F., and R.M. designed the experiments and analyzed the data. M.L. and R.M. wrote the paper. M.L., Y.F., Y.L., R.H., Y. Zhang, and Y. Zhao performed the experiments. All the authors discussed the results and commented on the manuscript. **Competing interests:** R.M., M.L., and Y.F. are applying for a patent related to this work. The other authors declare that they have no competing interests. **Data and materials availability:** All data needed to evaluate the conclusions in the paper are present in the paper and/or the Supplementary Materials.

Submitted 10 August 2023
Accepted 7 February 2024
Published 13 March 2024
10.1126/sciadv.adk2444